



Contents lists available at ScienceDirect

Neuroscience Research

journal homepage: www.elsevier.com/locate/neures



GABAergic inhibition reduces the impact of synaptic excitation on somatic excitation

Chiaki Kobayashi^a, Kazuki Okamoto^a, Yasuhiro Mochizuki^b, Hidetoshi Urakubo^c, Kenta Funayama^a, Tomoe Ishikawa^a, Tetsuhiko Kashima^a, Ayako Ouchi^a, Agnieszka F. Szymanska^d, Shin Ishii^c, Yuji Ikegaya^{a,e,*}

^a Laboratory of Chemical Pharmacology Graduate School of Pharmaceutical Sciences, The University of Tokyo, Bunkyo-ku, Tokyo, 113-0033, Japan

^b Laboratory for Integrated Theoretical Neuroscience, RIKEN Center for Brain Science, 2-1 Hirosawa, Wako, Saitama, 351-0198, Japan

^c Department of Systems Science, Graduate School of Informatics, Kyoto University, Sakyo-ku, Kyoto, 606-8501, Japan

^d Department of Biomedical Engineering, University of California, Irvine, USA

^e Center for Information and Neural Networks, National Institute of Information and Communications Technology, Suita City, Osaka, 565-0871, Japan

ARTICLE INFO

Article history:

Received 20 April 2018

Received in revised form 26 August 2018

Accepted 18 September 2018

Available online xxx

Keywords:

Calcium imaging

Patch-clamp recording

Synapse

Spine

Dendrite

Neuron

ABSTRACT

The effect of excitatory synaptic input on the excitation of the cell body is believed to vary depending on where and when the synaptic activation occurs in dendritic trees and the spatiotemporal modulation by inhibitory synaptic input. However, few studies have examined how individual synaptic inputs influence the excitability of the cell body in spontaneously active neuronal networks mainly because of the lack of an appropriate method. We developed a calcium imaging technique that monitors synaptic inputs to hundreds of spines from a single neuron with millisecond resolution in combination with whole-cell patch-clamp recordings of somatic excitation. In rat hippocampal CA3 pyramidal neurons *ex vivo*, a fraction of the excitatory synaptic inputs were not detectable in the cell body against background noise. These synaptic inputs partially restored their somatic impact when a GABA_A receptor blocker was intracellularly perfused. Thus, GABAergic inhibition reduces the influence of some excitatory synaptic inputs on the somatic excitability. Numerical simulation using a single neuron model demonstrates that the timing and locus of a dendritic GABAergic input are critical to exert this effect. Moreover, logistic regression analyses suggest that the GABAergic inputs sectionalize spine activity; that is, only some subsets of synchronous synaptic activity seemed to be preferably passed to the cell body. Thus, dendrites actively sift inputs from specific presynaptic cell assemblies.

© 2018 Elsevier B.V. and Japan Neuroscience Society. All rights reserved.

1. Introduction

Dendrites collect excitatory synaptic inputs and thereby excite the neuronal cell body (Eccles, 1964). When the summed synaptic inputs depolarize the membrane potential to the spike threshold, the neuron generates an action potential. However, this simple scheme may not fully illustrate the actual synaptic integration that occurs in real situations. Synaptic inputs attenuate during their

conduction along dendritic branches according to the cable theory, and dendrites dampen synaptic inputs due to their leaky cable properties, which are attributed to the expression of ion channels, such as potassium channels or chloride channels, opened by inhibitory synaptic inputs. Moreover, dendrites have highly elaborate arborized branching patterns (Mainen and Sejnowski, 1996) and express a variety of active receptors and ion channels (Migliore and Shepherd, 2002). Thus, the impact of an excitatory dendritic input on the cell body varies depending on where and when the input occurs (Mainen and Sejnowski, 1996; Reyes, 2001). Moreover, dendrites are likely to integrate excitatory inputs in a spatiotemporally complex manner (London and Hausser, 2005; Major et al., 2013; Spruston, 2008; Stuart and Spruston, 2015) and enable the postsynaptic neuron to diversify the spike outputs.

It is unclear how individual synaptic inputs affect the somatic membrane potential mainly because no experiments have simul-

Abbreviations: AP5, D-2-amino-5-phosphonopentanoic acid; CNQX, 6-cyano-7-nitroquinoxaline-2,3-dione; E_{Cl^-} , chloride ion equilibrium potential.

* Corresponding author at: Laboratory of Chemical Pharmacology Graduate School of Pharmaceutical Sciences, The University of Tokyo, 7-3-1 Hongo, Bunkyo-ku, Tokyo, 113-0033, Japan.

E-mail address: yuji@ikegaya.jp (Y. Ikegaya).

<https://doi.org/10.1016/j.neures.2018.09.014>

0168-0102/© 2018 Elsevier B.V. and Japan Neuroscience Society. All rights reserved.

taneously recorded synaptic and somatic excitation under natural conditions. Some synaptic inputs overcome the dendritic filtering to depolarize the somatic membrane potential, whereas not all synaptic inputs may influence the somatic membrane potential. Previous studies have addressed the faithfulness of synaptic conduction in somatic excitation using loose patch-clamp recording from a single spine and whole-cell recording from the soma (Forti et al., 1997). However, these studies isolated synaptic terminals and did not address the dynamic synapse-soma link under natural excitatory synaptic bombardments. It remains challenging to monitor synaptic activity in a single neuron that receives synaptic inputs from naturally spiking upstream neurons.

In the present work, we introduced a functional technique that captures the calcium activity from hundreds of dendritic spines in a neuron belonging to a spontaneously active network with a millisecond-resolution in combination with the whole-cell recording of somatic excitatory postsynaptic currents (EPSCs). We then examined how individual activity at each synapse affects the electrophysiological dynamics of the cell body. As a result, we found that a fraction of the spine activity was undetectable in the cell body against background noise, at least partly because of GABAergic inhibition. Moreover, this synaptic silencing seems to act as a filter that preferably passes synaptic inputs from specific cell assemblies to the soma.

2. Materials and methods

2.1. Ethical approval and animals

The experiments were performed with the approval of the animal experiment ethics committee at the University of Tokyo (approval no. P24-4, P24-5, P24-8, and P26-5) and according to the University of Tokyo guidelines for the care and use of laboratory animals. C57BL/6J mice and Wistar/ST (SLC, male or female) rats were housed in cages under standard laboratory conditions (12-h light/dark cycle, *ad libitum* access to food and water). All efforts were made to minimize the animals' suffering and the number of animals used.

2.2. Slice culture preparation

Entorhinal-hippocampal organotypic slices were prepared from Wistar/ST rats (7 postnatal days) as previously described (Koyama et al., 2007; Sasaki et al., 2011). Rat pups were anaesthetized with hypothermia and isoflurane and subsequently decapitated. The brains were removed and placed in ice-cold oxygenated Gey's balanced salt solution supplemented with 25 mM glucose. The brains were sliced horizontally (300- μ m thick) using a vibratome (DTK-1500, Dosaka), and the entorhinal-hippocampal regions were trimmed using a surgical microknife. The slices were placed on Omnipore membrane filters (JHWP02500, Millipore) and incubated in 5% CO₂ at 35 °C. The culture medium, which was composed of 50% minimal essential medium (Invitrogen), 25% Hanks' balanced salt solution, 25% horse serum (Gibco), and antibiotics, was changed every 3.5 days. Experiments were performed at 11–19 days *in vitro*. Slices were mounted in a recording chamber and perfused at a rate of 1.5–3 ml/min with oxygenated artificial cerebrospinal fluid (aCSF) that consisted of (in mM) 127 NaCl, 26 NaHCO₃, 3.5 KCl, 1.24 NaH₂PO₄, 1.3 MgSO₄, 2.4 CaCl₂, 10 glucose, and 0.4 Trolox.

2.3. Acute slice preparation

Acute slices were prepared from the hippocampus of male mice (4–6 postnatal weeks). The mice were anaesthetized with isoflurane and subsequently decapitated. The brains were removed and placed in ice-cold oxygenated solution that consisted of (in

mM) 222.1 sucrose, 27 NaHCO₃, 1.4 NaH₂PO₄, 2.5 KCl, 1 CaCl₂, 7 MgSO₄, and 0.5 ascorbic acid. The brains were sliced at a thickness of 400 μ m horizontally for the hippocampus using a VT1200S vibratome (Leica). The slices were allowed to recover at room temperature for at least 1.5 h while submerged in a chamber filled with oxygenated aCSF consisting of (in mM) 127 NaCl, 26 NaHCO₃, 1.6 KCl, 1.24 KH₂PO₄, 1.3 MgSO₄, 2.4 CaCl₂, and 10 glucose. The slices were mounted in a recording chamber and perfused at a rate of 1.5–3 ml/min with oxygenated aCSF.

2.4. In vitro electrophysiology

All recordings were performed at 32–33 °C. Whole-cell recordings were collected from two hippocampal CA3 pyramidal neurons using a MultiClamp 700B amplifier and a Digidata 1550 digitizer controlled by pCLAMP 10.5 software (Molecular Devices). Borosilicate glass pipettes (3–6 M Ω) were filled with a solution containing (in mM) 130 CsMeSO₄, 10 CsCl, 10 HEPES, 10 phosphocreatine, 4 MgATP, 0.3 NaGTP, and 10 QX-314. Paired whole-cell recordings were performed in two neurons located at an interneuron interval of less than 100 μ m; one glass pipette contained 200 μ M picrotoxin. The recorded cells were visualized using 100 μ M Alexa Fluor 488 hydrazide or Alexa Fluor 568 hydrazide added to the intracellular solution with a Nipkow-disk confocal unit (CSUX-1, Yokogawa Electric), a CMOS camera (ORCA-Flash4.0 V2, Hamamatsu Photonics), a water-immersion objective lens (16 \times , 0.80 numerical aperture, Nikon) and image acquisition software (HSR, Hamamatsu Photonics). Liquid junction potentials were not corrected. The signals were low-pass filtered at 1 kHz and digitized at 20 kHz.

2.5. In vivo electrophysiology

Male mice (5–6 postnatal weeks) were anaesthetized with ketamine (50 mg/kg, *i.p.*) and xylazine (10 mg/kg, *i.p.*). Anesthesia was confirmed by a lack of paw withdrawal, whisker movement, and eye blink reflexes. The head skin was subsequently removed, and the animal was implanted with a metal head-holding plate. After 2 days of recovery, the mice received head-fixation training on a custom-made stereotaxic fixture for 1–3 h per day until they learned to remain quiet. After full habituation, the mice were anaesthetized with ketamine/xylazine. A craniotomy (1 \times 1 mm²) centered at 3.5 mm posterior to Bregma and 2.0 mm ventrolateral to the sagittal suture was performed, and 0.2% lidocaine was applied to the surgical region for analgesia. The dura was surgically removed. The exposed cortical surface was covered with 1.8% agar at a thickness of 0.5 mm. A heating pad maintained the rectal temperature at 37 °C throughout the experiments. Recordings were initiated 30–50 min after recovery from anesthesia. Borosilicate glass pipettes (3.3–5.8 M Ω) were filled with a solution containing (in mM) 130 CsMeSO₄, 10 CsCl, 10 HEPES, 10 phosphocreatine, 4 MgATP, 0.3 NaGTP, 3 QX-314, 0.05 Alexa Fluor 594, and 0.2% biocytin. One of the two glass pipettes used in the paired whole-cell recordings contained 200 μ M picrotoxin. One pipette was lowered perpendicularly and the other at an angle of 30 degrees into the primary visual cortex with an electric manipulator (DMX-11, Narishige). Paired recordings were collected from layer 2/3 neurons at depths of 150–350 μ m from the pia using a MultiClamp 700B amplifier and a Digidata 1440 A digitizer controlled by pCLAMP 10.1 software. Data in which the series resistance exceeded 65 M Ω or changed by more than 15% during the recording session were discarded. For each neuron, spike responses to an injection of brief inward currents were examined, and regular spiking neurons were considered putative pyramidal cells and used in the subsequent analyses (Funayama et al., 2015). The signals were low-pass filtered at 2.0 kHz and digitized at 20 kHz. The recorded area was confirmed by *post hoc* imaging of intracellularly loaded Alexa 594, which was

dissolved at 100 μM in the intrapipette solution. The total periods of recording were restricted to less than 60 min to minimize stress in the animals.

2.6. Calcium imaging of spines

All recordings were performed at 32–33 °C. Hippocampal CA3 pyramidal neurons were patch-clamped using a MultiClamp 200B amplifier and a Digidata 1440 A digitizer controlled by pCLAMP 10.3 software (Molecular Devices). Glass pipettes were filled with a solution containing (in mM) 47.7 CsMeSO₄, 92.3 CsCl, 10 HEPES, 10 phosphocreatine, 4 MgATP, 0.3 NaGTP, 10 QX-314, and 0.2 fluo-4. Note that the concentration of chloride ions in the intrapipette solution was increased at $E_{\text{Cl}^-} = -10$ mV to mainly record EPSCs at -30 mV (Fig. 2A and B). Calcium events in spines were more reliably detected when patched neurons were more depolarized (Fig. 2D) most likely because the calcium entry into spines was mediated mainly by NMDA receptor channels (Fig. 2E). Therefore, in this study, voltage-clamp recordings were conducted at -30 mV. This was also the reason why we chose the voltage-clamp configuration instead of the current-clamp mode. The signals were increased 5–10-fold to minimize internal noise, low-pass filtered at 1 kHz and digitized at 20 kHz. In some experiments, the glass pipette contained 200 μM picrotoxin. Images were acquired at 100–333 frames per second with a Nipkow-disk confocal unit (CSUX-1, Yokogawa Electric), a CMOS camera (ORCA-Flash4.0 V2, Hamamatsu Photonics), a water-immersion objective lens (60 \times , 1.0 numerical aperture, Nikon) and image acquisition software (HSR, Hamamatsu Photonics). The fluorophore was excited at 488 nm (0.2–0.4 mW) with an argon-krypton laser (641-YB-A01; Melles Griot) and visualized using 500 nm long-pass emission filters. At the end of each experiment, images were captured at a Z step of every 1 μm . In the three-dimensional image, the spines, their belonging dendritic shafts, and the morphology of the dendrites were manually measured. In each spine, the fluorescence change $\Delta F/F$ was calculated as $(F_t - F_0)/F_0$, where F_t was the fluorescence intensity at frame time t , and F_0 was the baseline. The baseline was calculated as the average of the minimal 3% values in the fluorescence intensities during a period of ± 5 s relative to time t . Note that the synaptic activity was temporally sparse; thus, this definition was not affected by the synaptic activity. More detailed information regarding the definition and detection threshold of calcium transients is described elsewhere (Szymanska et al., 2016).

2.7. Super-resolution image acquisition

To visualize the subcellular structures of cells, calcium imaging was performed using glass pipettes containing 100 μM Alexa Fluor 568 hydrazide or 0.2% biocytin. After each experiment, the glass pipette was carefully detached from the recorded neuron. Slices were fixed with 4% PFA in phosphate-buffered saline (PBS) at room temperature overnight and then washed three times with PBS. To visualize biocytin, the slices were incubated with 0.2% Triton X-100 and streptavidin-Alexa Fluor 594 conjugate (1:500). Super-resolution images were acquired using the FV-OSR system (Olympus) mounted on an FV1200 or FV1000 confocal microscope with an oil-immersion objective lens (100 \times , 1.4 numerical aperture) using Fluoview image acquisition software (Olympus). Alexa Fluor 568 was excited with a 559-nm laser. Alexa Fluor 594 was excited with a 561-nm laser. The spines were identified in the super-resolution images using ImageJ and neuroLucida360. The spine head volume was estimated as $4\pi(\varphi/2)^3/3$, in which φ represents the head width of the spine. The head width was measured from the maximum spine area of the Z-step images (0.5–1 μm

steps). The spine neck length was measured as the distance from the center of gravity of the spine head to the stem dendrite.

2.8. Computational modeling

Shunting inhibition in a hippocampal CA3 pyramidal neuron was simulated using the NEURON simulation environment (v7.3) (Hines and Carnevale, 1997). We used a morphologically detailed model of the CA3 pyramidal neuron that consisted of 1213 electrical compartments with uniform passive properties ($C_m = 1.41$ $\mu\text{F cm}^{-2}$; $R_m = 25.37$ $\text{k}\Omega \text{ cm}^2$; $R_a = 50$ $\Omega \text{ cm}$ in the axon and 150 $\Omega \text{ cm}$ in the other parts) (Safuulina et al., 2010). This model incorporated various voltage- or calcium-dependent ionic currents: two types of Na^+ currents, five types of potassium currents (delayed rectifier, K_v7 , A-type, calcium-activated and afterhyperpolarization), L-type, N-type and T-type calcium currents and a nonspecific I_h current. Simple intracellular calcium dynamics were modeled for the calcium-activated potassium current, and the resting potential was set to -70 mV. We modeled AMPA and NMDA receptor currents in response to a glutamate signal. The kinetics of the currents were based on the literature (Baker et al., 2011), and the reversal potentials were set to 0 mV. The peak conductances of the AMPA and NMDA receptor currents were set to 1.0 nS and 0.2 nS, respectively. These conductances produced a 0.226 mV excitatory postsynaptic potential and a -9.7 pA EPSC (holding potential: -70 mV) in the soma, where the glutamate signal was given to an apical dendritic branch (406 μm away from the soma). This excitation did not cause a dendritic spike. We also modeled a GABAergic current in response to the GABA signal. The GABAergic current had double exponential kinetics with rise and decay time constants of 1.4 ms and 12.5 ms, respectively. The reversal potential of the GABAergic current was set to -70 mV, and the peak conductance was set to 10 nS unless otherwise indicated. This conductance produced a 5.7 pA somatic inhibitory postsynaptic current (IPSC; holding potential: 0 mV), in which the location of the GABA signal was the same as that of the glutamate signal. The decay time constant was 20 ms, consistent with experimental evidence (Liu, 2004). The NEURON function SEClamp was used for voltage clamp simulation ($r_s = 0.01$ $\text{M}\Omega$). The ratio of the EPSC+IPSC integral over the EPSC integral was measured from the soma.

2.9. Clustering of spines with affinity propagation

Spines with excess synchronous activity were grouped by the affinity propagation clustering algorithm (Frey and Dueck, 2007; Takahashi et al., 2010). Given a set of points and a set of similarity values between the points, affinity propagation identifies clusters of points with high similarities, and a representative point referred to as the “exemplar” is automatically allocated for each cluster. For each point, a scalar value referred to as the ‘preference’, which is a measure of how likely the point is to be chosen as an exemplar, is arbitrarily set, and these scalar values are adjusted for the resulting number of clusters. Here, we defined the similarity measures between each pair of spines as the total number of the synchronized calcium events of the pair and clustered observed spines into spine sets. We set the values of preference to be equal for all points and adjusted the value to provide 5 spine sets. If there was no solution with 5 clusters with the equal preference setting, the preference that gave the number of spine sets nearest to five was selected; some data were clustered into 4–8 spine sets.

2.10. Bayesian logistic regression model

A Bayesian logistic regression model was adopted to statistically describe the stochastic influences of spine activity on the soma. We introduced a prior distribution to avoid overfitting due to the finite

size of the activity series, and the model parameters were estimated with the maximum *a posteriori* (MAP) method. We discretized 120 s of a recording period into segments of 30 ms. Let $t = 1, \dots, T$ be the index of a time bin. Using $x_{t,i}^n$, we denote the activity of the spine i in the spine set n (prefixed by affinity propagation) at the time bin t , where $x_{t,i}^n$ is an indicator variable that equals 1 if there is spine activity at time t and 0 otherwise. The occurrence probability of a somatic EPSC at time t (π_t) is related to the spine activity $x_{t,i}^n$ by a logistic regression model with:

$$\log \frac{\pi_t}{1 - \pi_t} = \alpha + \sum_n \left[\beta_n \sum_i x_{t,i}^n \right]. \quad (1)$$

The first term α models the effect of the activity of unobserved spines on the occurrence of a somatic EPSC, and the second term models the effect of the activity in spine set n on the occurrence of a somatic EPSC with magnitude β_n . Let y_t denote the observed response variable, where y_t has a value of 1 if a somatic EPSC is observed at the time bin t and 0 otherwise. Assuming that the occurrence of a somatic EPSC in each time bin obeys a Bernoulli distribution, the log likelihood function may be written as follows:

$$\log p(y_t | \alpha, \beta_n) = \sum_t y_t \log \pi_t + (1 - y_t) \log(1 - \pi_t). \quad (2)$$

We choose a prior distribution for the parameter β_n to be a Gaussian distribution with zero mean:

$$p(\beta_n) = \frac{1}{\sqrt{2\pi\sigma^2}} e^{-\beta_n^2/2\sigma^2}, \quad (3)$$

where the standard deviation σ is set to be equal for all spine sets. Then, a MAP estimate of the parameters was obtained by maximizing the log posterior probability function or, equivalently, by minimizing the L2 regularized negative log likelihood function:

$$L(\alpha, \beta_n) = -\sum_t y_t \log \pi_t + (1 - y_t) \log(1 - \pi_t) + \frac{1}{2\sigma^2} \sum_n \beta_n^2. \quad (4)$$

The optimal value of σ was determined by 5-fold cross-validation together with the one standard error rule (Hastie et al., 2009), and Eq. (4) was minimized using the method of iterative reweighted least squares.

2.11. Test for the linearity of the summation of spine activity

To test whether synchronous spine activity affects the EPSC probability in a nonlinear manner, we compared the logistic regression model that accounts for only a linear effect on EPSC occurrence (Eq. (1)) to the model that also accounts for a nonlinear effect due to synchronous spine activity:

$$\log \frac{\pi_t}{1 - \pi_t} = \alpha + \sum_n \left[\beta_n \sum_j x_{t,j}^n \right] + \sum_n \left[\gamma_n \sum_{i < j} x_{t,i}^n x_{t,j}^n \right], \quad (5)$$

where the parameter γ_n models the nonlinear effect on somatic EPSC occurrence due to a synchronous activity of the intragroup spine pair from the spine set n . We then performed model selection separately for each data set using the Bayesian information criterion (BIC). For a given model \mathcal{M} , BIC is defined as follows:

$$BIC = -2 \log p(y_t | \hat{\theta}, \mathcal{M}) + k \log T, \quad (6)$$

where $\hat{\theta}$ is an MAP estimate of the parameters of \mathcal{M} , k is the number of parameters and T is the number of time bins. The value of BIC approximates twice the negative log marginal likelihood $-2 \log p(y_t | \mathcal{M})$. Therefore, minimizing the model, the BIC value indicates a better description of the data (Hastie et al., 2009).

2.12. Data analysis and representation

Data were analyzed using custom-made codes in ImageJ, neuroLucida360 and MATLAB. Summarized data are reported as the means \pm SDs unless otherwise specified.

3. Results

3.1. Some spine activities induce undetectable EPSCs in the soma against background noise

We loaded CA3 pyramidal cells in cultured hippocampal slices with 200 μ M fluo-4, a fluorescent calcium indicator, through somatic patch-clamp pipettes and optically recorded the spontaneous calcium activity from individual spines in a 187×122 - μ m² field of a spinning-disk confocal microscope (Fig. 1A). Because cultured slices have transparent parenchyma, we could simultaneously monitor, on average, 220 ± 78 spines from a single cell (mean \pm SD of 24 videos taken from 24 neurons, ranging from 128 to 428 spines) at 100–333 frames per second. The spatial distributions of the imaged spines are plotted in Fig. 1B and C; the spines were located at the mean path distance of 82.9 ± 32.1 μ m from the soma along the dendrites (Fig. 1B), and the path distance between two given spines was 120.5 ± 54.7 μ m (Fig. 1C). In total, 4457 of 5279 spines (84.4%) showed spontaneous calcium activity during the observation period of 180–300 s. The mean frequency of calcium events was 2.2 ± 1.2 per minute. The cross-correlogram of the calcium event timings between different spines exhibited a peak at 0 s (Fig. 1D top), indicating that dendrites receive synchronous synaptic inputs. Indeed, the majority of the EPSCs recorded in the soma had larger amplitudes than those expected for single synaptic inputs (e.g., Figs. 1A, 2A, 3A, and 5F).

To reliably detect NMDA receptor-dependent synaptic calcium events, we adopted a voltage-clamp configuration and voltage-clamped the patched neurons at -30 mV throughout the experiments. We also modified the intrapipette concentration of chloride ions so that somatic EPSCs dominated the recorded currents (Fig. 2A); note that upward postsynaptic currents were recorded under the theoretical chloride ion (E_{Cl^-}) equilibrium potential of -30 and -20 mV but disappeared under $E_{Cl^-} = -10$ mV, in which the downward postsynaptic currents were abolished by bath perfusion with a cocktail of ionotropic glutamate receptor antagonists (Fig. 2B). Although the EPSC frequency observed at -30 mV did not differ significantly from that at -70 mV (Fig. 2C), the spine calcium events were reduced at lower clamped voltages (Fig. 2D) and were abolished by 50 μ M D-2-amino-5-phosphonopentanoic acid (AP5), an NMDA receptor antagonist (Fig. 2E). Therefore, we concluded that these calcium events reflected excitatory synaptic activity-mediated calcium influx through NMDA receptor channels.

The cross-correlogram of the event timings between the spine calcium activity and the recorded EPSCs peaked at 0 s (Fig. 1D bottom), indicating that, as a whole, synaptic inputs readily excited the soma. However, when we compared the event timings of individual spine activity to those of individual EPSCs (Fig. 3A), we unexpectedly discovered that, in a fraction of spine activity, EPSCs were not detectable against background noise. For each spine calcium activity, if the activity occurred simultaneously with a detectable EPSC, it was defined as an “effective input”; note that an EPSC event was considered when its amplitude exceeded the background current noise amplitude (7 pA) and the time window allowed for the simultaneity between the spine activity and the EPSC was 30 ms, which typically corresponded to 3 video frames. As an example, EPSC-coupled spine activity is displayed as red dots in a raster plot in Fig. 3B. The probabilities that calcium events were accompanied

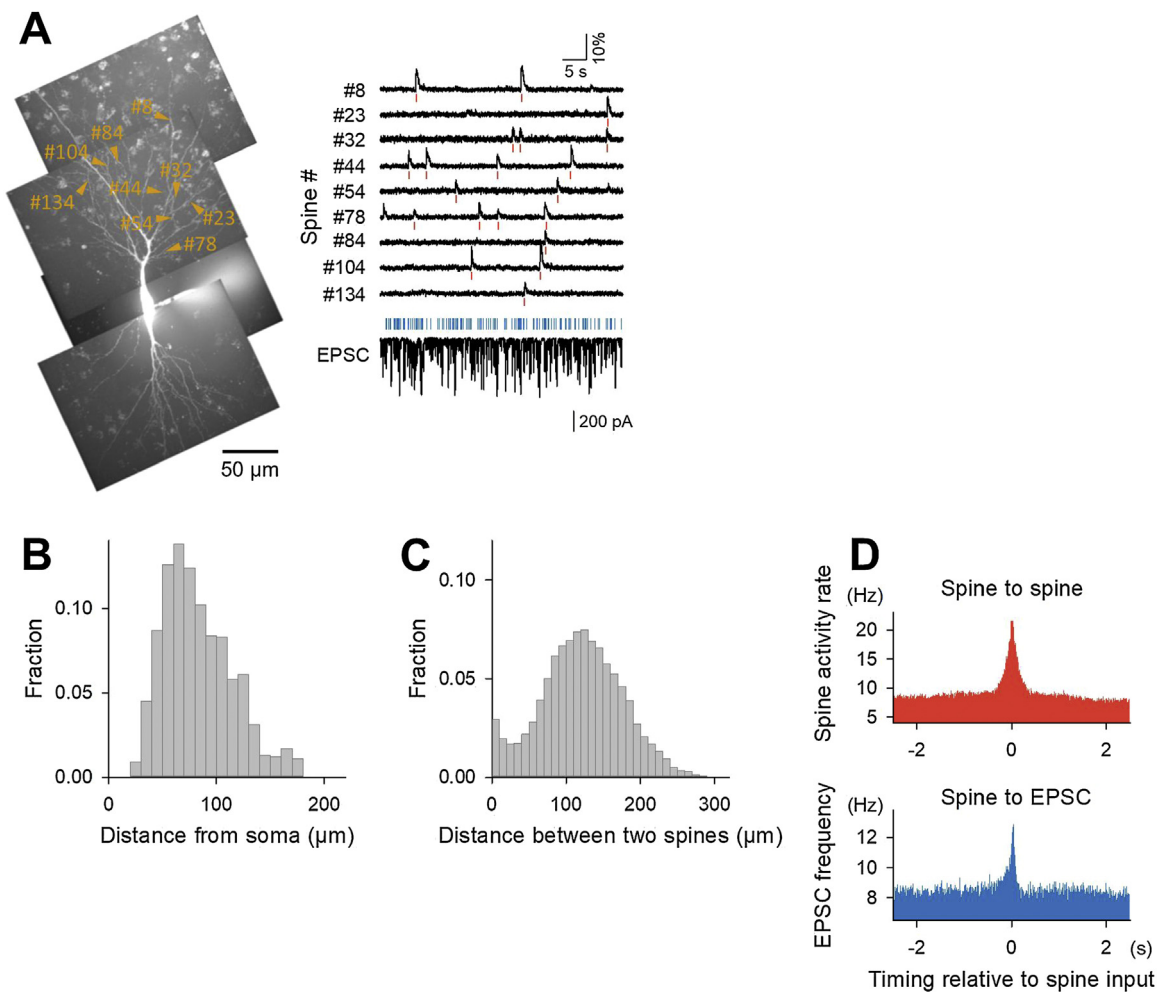


Fig. 1. High-speed calcium imaging of synaptic activities. (A) Raw traces of the spontaneous calcium activity of nine representative spines in a neuron (top) and spontaneous EPSCs recorded from the soma of the same neuron (bottom, $V_h = -30$ mV). Images were captured at 333 frames per second (frame duration = 3 ms). The bars below the calcium trace or EPSC trace indicate the onset times of calcium events or EPSCs. (B) Distribution of the locations of observed spines for the distance from the soma. $n = 1001$ spines in 9 neurons. (C) Same as B but for the distance between two spines. $n = 68,005$ pairs in 9 neurons. (D) Cross-correlations of event timings between calcium activity of different spines (top) and between spine activity and EPSCs (bottom). $n = 14,585$ calcium events in 2811 spines from 15 control neurons.

by detectable EPSCs, referred to herein as EPSC probabilities, were heterogeneous across spines (Fig. 3B right and C). We calculated the EPSC probabilities of all spines that exhibited more than four calcium events during the recording periods. The average EPSC probability was $52.0 \pm 19.5\%$ (mean \pm SD of 1282 spines from 15 control videos).

To understand the difference between the spine activity accompanied by detectable EPSCs (effective inputs) and that unaccompanied by detectable EPSCs (ineffective inputs), we conducted a further analysis. The EPSC probabilities were not correlated with the event frequencies of the spine activity (Fig. 4A, $r = 0.035$) or the path distances from the soma to the spines along the dendrites (Fig. 4B, $r = 5.1 \times 10^{-4}$). Moreover, the differences in the EPSC probabilities between all possible pairs of the spines did not depend on the path distances between them (Fig. 4C left, $r = 0.013$). This tendency held true when spine pairs on the same dendritic branches (Fig. 4C middle, $r = 0.086$) or across different branches (Fig. 4C right, $r = 0.030$) were separately plotted. We have previously demonstrated that spontaneous synaptic inputs tend to be locally synchronized (Takahashi et al., 2012). Interestingly, the distributions of the distances between two nearest coactive spines were slightly shorter for effective input pairs than for ineffective input pairs (Fig. 4D; $P = 6.8 \times 10^{-8}$, $D_{1,817} = 0.13$, Kolmogorov–Smirnov test, $n = 1065$ effective synchronizations and 753 ineffective syn-

chronizations in 15 neurons), indicating that effective inputs were more spatially clustered than ineffective inputs and reflecting that clustered inputs can more efficiently influence the somatic membrane potential presumably because of their nonlinear integration (Iacaruso et al., 2017; Losonczy and Magee, 2006; Takahashi et al., 2012). However, even for ineffective inputs, 23.6% of them were clustered within $10 \mu\text{m}$. Therefore, another factor may also underlie the somatic influence of synaptic inputs.

Super-resolution microscopic inspection revealed that neither the head sizes nor the neck lengths of the spines were correlated with their EPSC probabilities (Fig. 4E and 4F, $r = 0.047$ and 0.073 , respectively). Therefore, the position or morphology of spines cannot explain the detectability of somatic EPSCs. The amount of calcium entry into spines may be determined by the strength of the synaptic inputs. Consistent with this notion, we found that the EPSC probabilities were weakly correlated with the amplitudes of the calcium transients (Fig. 4G). Moreover, even within the same spines, the amplitudes of the EPSC-detected calcium transients (effective inputs) were slightly but significantly larger than those of the EPSC-undetected calcium transients of the same spines (ineffective inputs) (Fig. 4H, $P = 9.4 \times 10^{-27}$, $t_{719} = 11.2$, paired t -test within-spine comparisons). However, these correlations were substantially weak; therefore, we conclude that the strength of

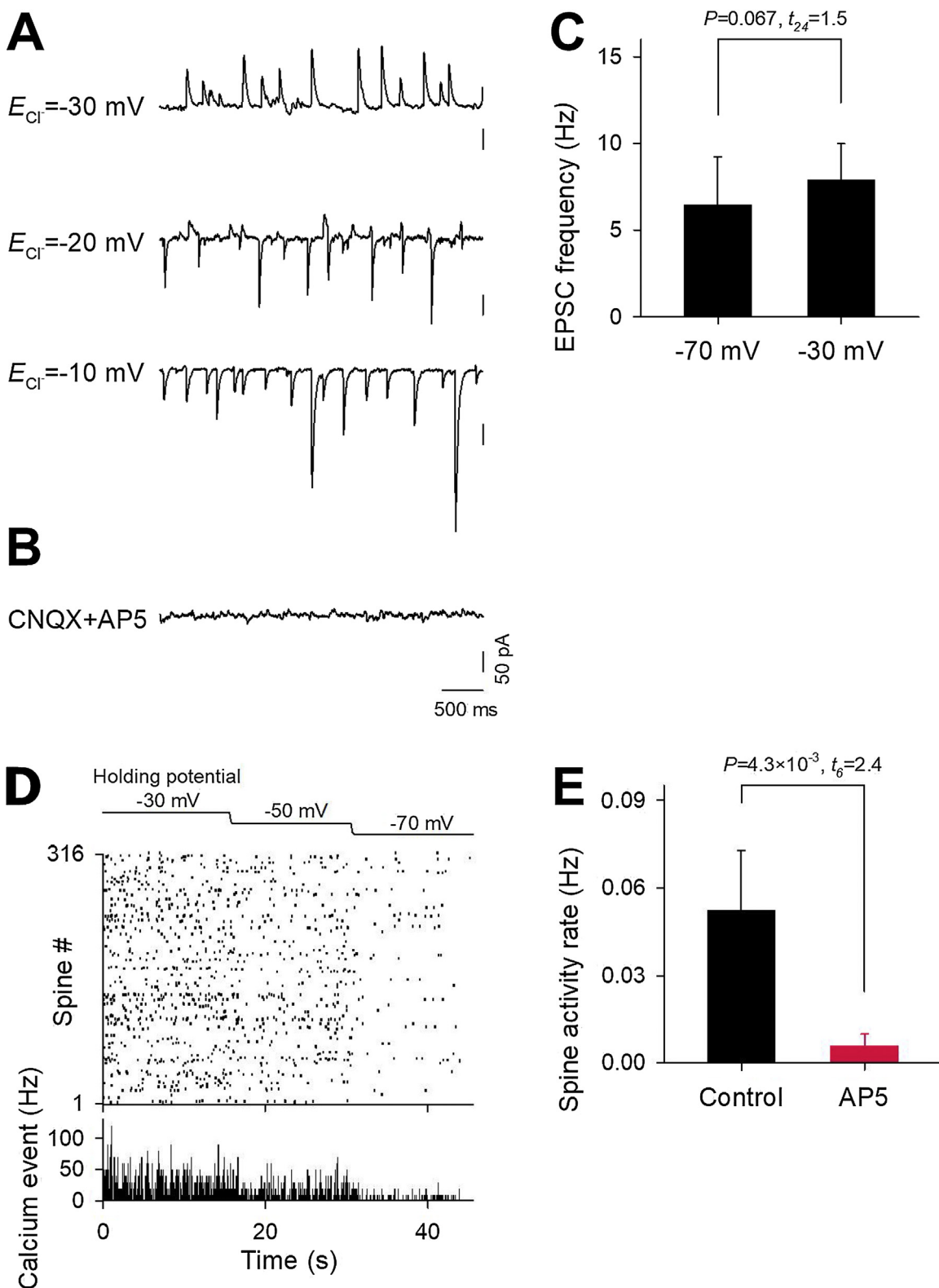


Fig. 2. Calcium activity in spines reflects synaptic activity. (A) Voltage-clamp recordings of postsynaptic currents in *ex vivo* CA3 hippocampal neurons at $V_h = -30$ mV under the chloride ion (E_{Cl^-}) theoretical equilibrium potential of -30 , -20 , and -10 mV, in which the liquid junction potential measured 2.8, 1.0, and 0.24 mV, respectively. Note that upward postsynaptic currents were recorded under $E_{Cl^-} = -30$ and -20 mV and disappeared under $E_{Cl^-} = -10$ mV. (B) Postsynaptic currents at $V_h = -30$ mV under $E_{Cl^-} = -10$ mV disappeared in the presence of $50 \mu\text{M}$ 6-cyano-7-nitroquinoxaline-2,3-dione (CNQX) and $50 \mu\text{M}$ D-2-amino-5-phosphonopentanoic acid (AP5) and thus reflected EPSCs. Note that the theoretical equilibrium potential of the chloride ion is not equal to the experimentally measured reversal potential of inhibitory postsynaptic currents, presumably because of imperfect space clamping or the conductance of bicarbonate through GABA_A receptor channels. (C) The EPSC frequencies were compared between neurons at $V_h = -30$ mV under $E_{Cl^-} = -10$ mV ($n = 15$ neurons) and at $V_h = -70$ mV under $E_{Cl^-} = -70$ mV ($n = 11$ neurons). The data represent the mean \pm SD. Student's *t*-test. (D) Spine calcium activity was more frequently detected when the neuron was clamped at higher voltages. *Top*: holding potentials of the voltage-clamp configuration; *Middle*: a raster plot of calcium events of 316 spines; and *Bottom*: time-histogram of calcium event frequencies. (E) Synaptic activity was reduced by bath application of $50 \mu\text{M}$ AP5, an NMDA receptor antagonist. The data represent the mean \pm SD of 4 control and 4 AP5-treated neurons. Student's *t*-test.

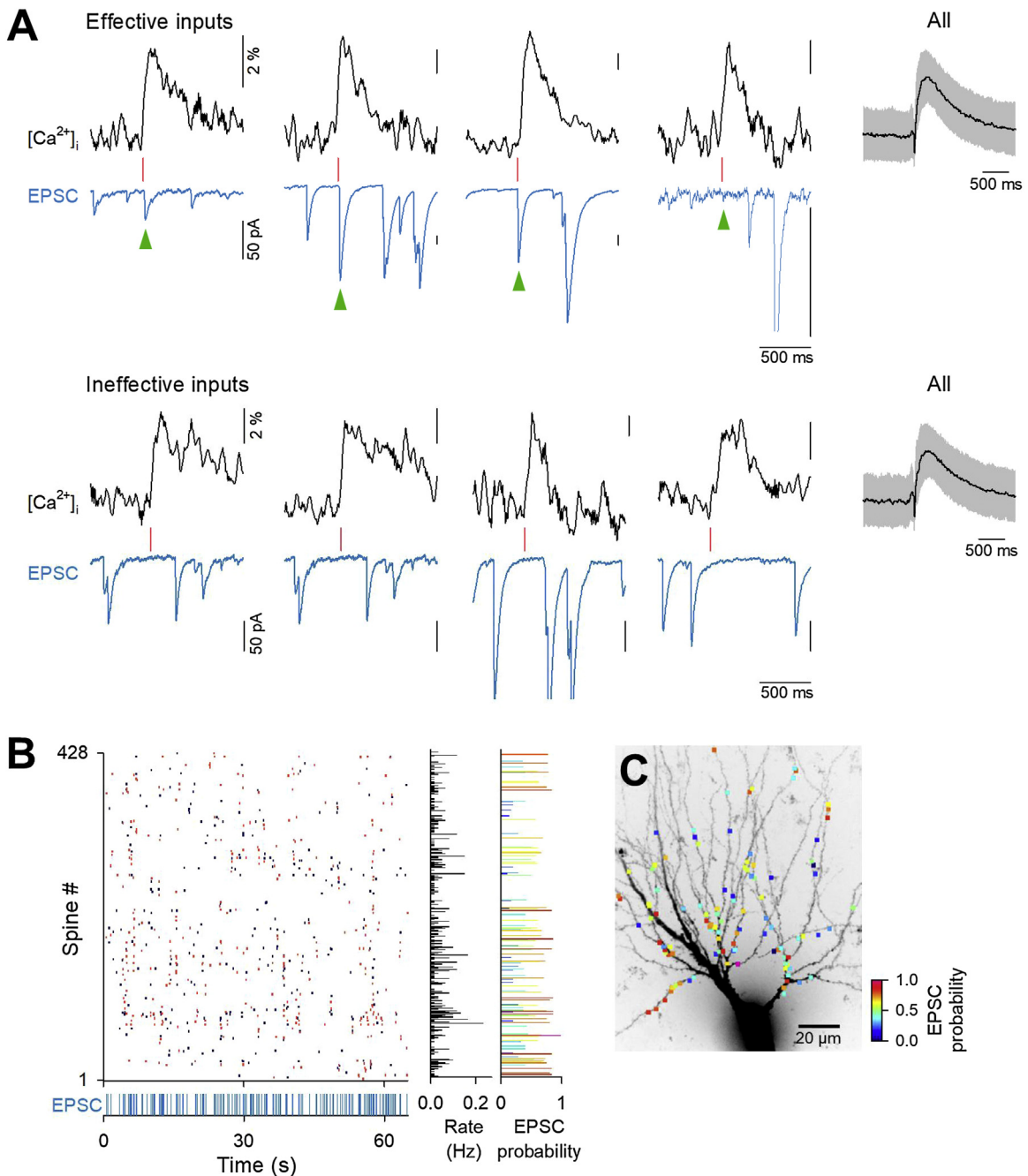


Fig. 3. Spine activity is sometimes undetected as somatic EPSCs. (A) Representative traces of EPSC-detected and EPSC-undetected calcium events. The traces represent calcium transients and EPSCs. The bars are the onsets of calcium transients. The arrows indicate EPSCs that occurred simultaneously with the calcium transients. Note that the left two calcium events in ineffective inputs occurred in two different spines at the same frame, which indicates that this synchronized activity did not induce detectable EPSCs in the cell body. In the traces furthest to the right, all calcium transients of spines were averaged relative to the onset timings of the calcium transients (mean \pm SD of 7311 effective and 7389 ineffective calcium transients from 15 neurons), which indicates that the waveform of the calcium transients did not differ between effective and ineffective events. (B) Raster plot of the calcium events of all 428 spines (top) and the EPSC times (bottom). The black and red dots represent EPSC-coupled and EPSC-uncoupled calcium events, respectively. The two right histograms display the frequencies of calcium events in individual spines and the probabilities that their calcium events occurred with detectable EPSCs. (C) The probabilities that their calcium events occurred with detectable EPSCs, shown in (B), are mapped onto the corresponding spines of a confocally imaged neuron in a pseudocolored scale.

synaptic inputs alone cannot fully explain the stochastic behavior of the EPSC occurrence.

3.2. Dendritic GABAergic inhibition reduces the somatic influence of synaptic activity

The amplitudes of the calcium transients in the dendritic shafts for the spine activity that induced detectable EPSCs were slightly

larger than those that induced undetectable EPSCs (Fig. 5A, $P = 3.1 \times 10^{-3}$, $t_{287} = 2.7$, Student's t -test); note that the calcium fluorescence change in the 5- μ m dendritic segment arising from a given spine protrusion during the calcium activity of the spine was measured as a calcium transient in the dendritic shaft. Although this fact implies that nonlinear integration occurred in these inputs, it is also possible that synaptic inputs are shunted by local dendritic inhibition

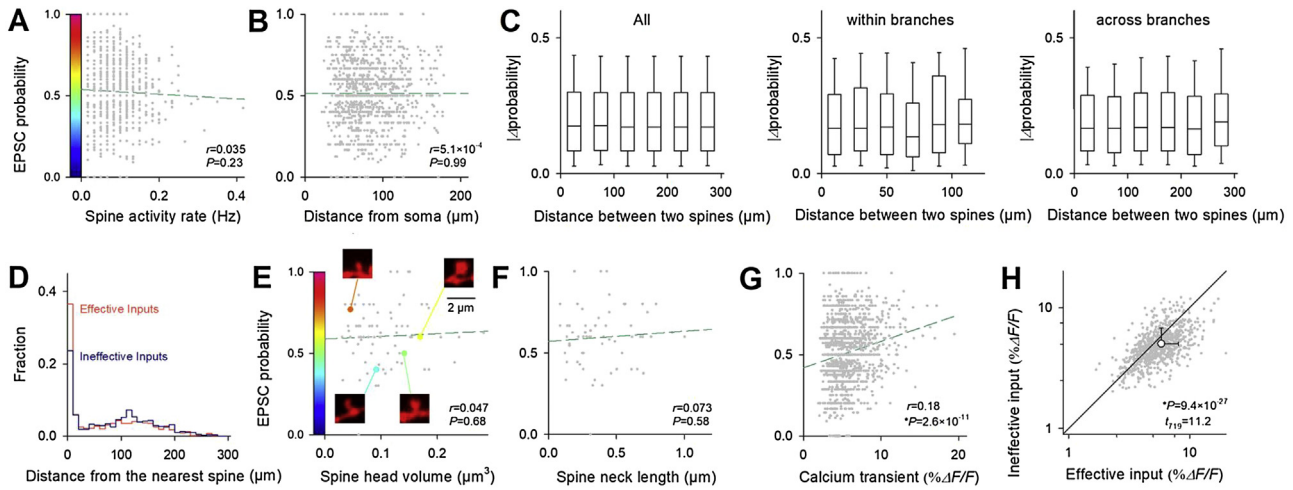


Fig. 4. EPSC-detected synaptic inputs induce larger calcium transients than EPSC-undetected inputs. (A–B) The EPSC probabilities were plotted against the spine activation rates and the path distance from the somata. Each dot represents a single spine. The dashed lines are least-square best fits (A, $n = 1135$ spines in 15 neurons; B, $n = 1001$ spines in 9 neurons). (C) The differences in EPSC probabilities between two spines were not correlated with the interspine path distance ($n = 68,005$ pairs in 9 neurons) (left). The differences in EPSC probabilities between either two spines on the same branches (middle, $n = 2738$ pairs) or across different branches (right, $n = 27,916$ pairs) were not correlated with the interspine path distance. (D) The distribution of the distances between any given pair of the nearest coactive spines among 1065 effective synchronizations and 753 ineffective synchronizations in 9 neurons. Each line indicates effective inputs and ineffective inputs, respectively. Kolmogorov-Smirnov test. (E–F) The EPSC probabilities were not correlated with the head size or neck length of the spines ($n = 61–79$ spines that could be identified *post hoc* in 8 superresolution images). The inset images display representative spines. (G) The EPSC probabilities were correlated with the amplitude of calcium transients ($n = 1281$ spines in 15 neurons). (H) Within each spine, the EPSC-detected calcium transients were nearly comparable to the EPSC-undetected transients in amplitude ($n = 720$ spines in 15 neurons). The black line is the diagonal line. We analyzed only spines that exhibited both EPSC-detected and EPSC-undetected calcium transients.

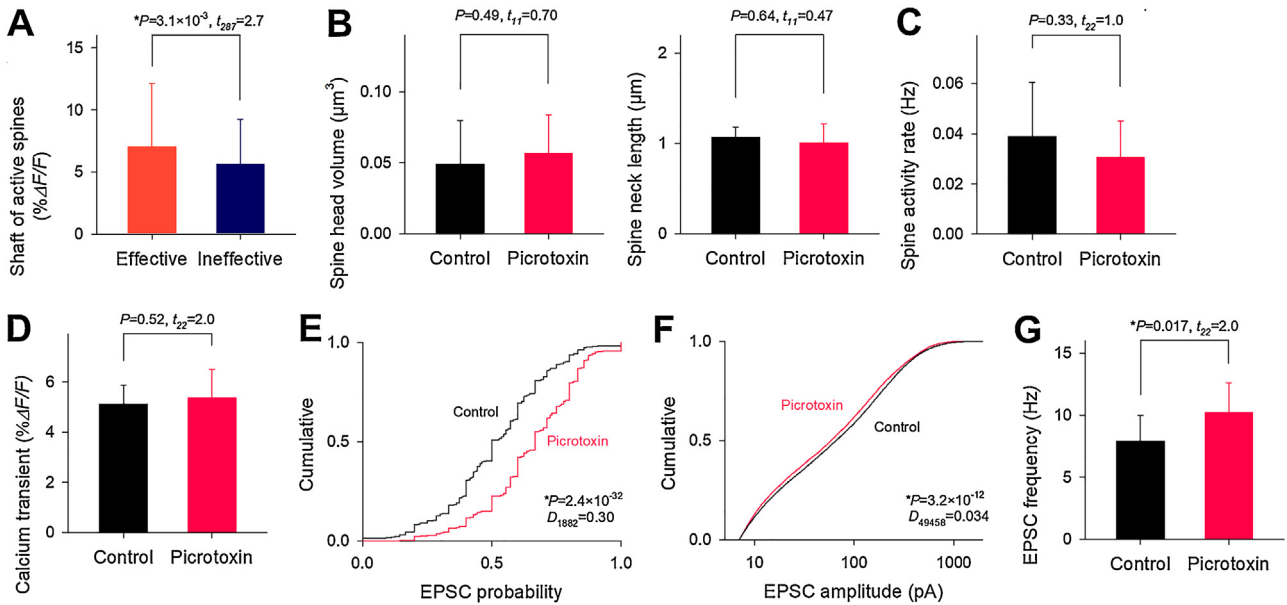


Fig. 5. Intracellular picrotoxin does not alter the properties of spine activity. (A) The amplitudes of calcium transients in dendritic shafts to which activated spines belonged were compared between effective and ineffective inputs. The data are shown as the mean \pm SD of 142 shafts in effective inputs and 147 shafts in ineffective inputs from 15 neurons. Student's *t*-test. (B) Comparison of the neck lengths (left) and head volumes of spines (right) between 6 control neurons and 7 picrotoxin-loaded neurons. The data represent the mean \pm SD. Student's *t*-test. (C) Comparison of the frequencies of spine activity between neurons intracellularly perfused with and without 200 μ M picrotoxin. The data represent the mean \pm SD of 15 control and 9 picrotoxin-injected neurons. Student's *t*-test. (D) Comparison of the amplitudes of calcium transients in spines between neurons intracellularly perfused with and without 200 μ M picrotoxin. The data represent the mean \pm SD of 15 control and 9 picrotoxin-injected neurons. Student's *t*-test. (E) Cumulative distributions of the EPSC probabilities of 1282 spines from 15 control neurons and 602 spines from 9 picrotoxin-loaded neurons. Kolmogorov-Smirnov test. In each spine, the corrected EPSC probability was calculated as the EPSC probability from which the chance level was deducted. (F) Cumulative distributions of the EPSC amplitudes of 30,985 events from 15 control neurons and 18,475 events from 9 picrotoxin-loaded neurons. Kolmogorov-Smirnov test. (G) The EPSC frequencies were compared between neurons intracellularly perfused with and without 200 μ M picrotoxin. The data represent the mean \pm SD of 15 control and 9 picrotoxin-injected neurons. Student's *t*-test.

(Liu, 2004). Therefore, we investigated whether GABAergic inputs in dendrites contribute to undetectable EPSCs.

If a fraction of synaptic inputs become undetectable by GABAergic inputs, they can restore their somatic impact by reducing GABAergic inputs. Thus, we intracellularly loaded neurons with picrotoxin, a GABA_A receptor channel blocker, to reduce the

GABAergic influence in the recorded cells (Inomata et al., 1988; Nelson et al., 1994; Yazaki-Sugiyama et al., 2009). The loading of picrotoxin did not affect the spine morphology (Fig. 5B). Moreover, it did not alter the frequency of calcium events (Fig. 5C) or the amplitude of the calcium transients in spines (Fig. 5D). However, the picrotoxin-loaded neurons exhibited higher EPSC probabilities

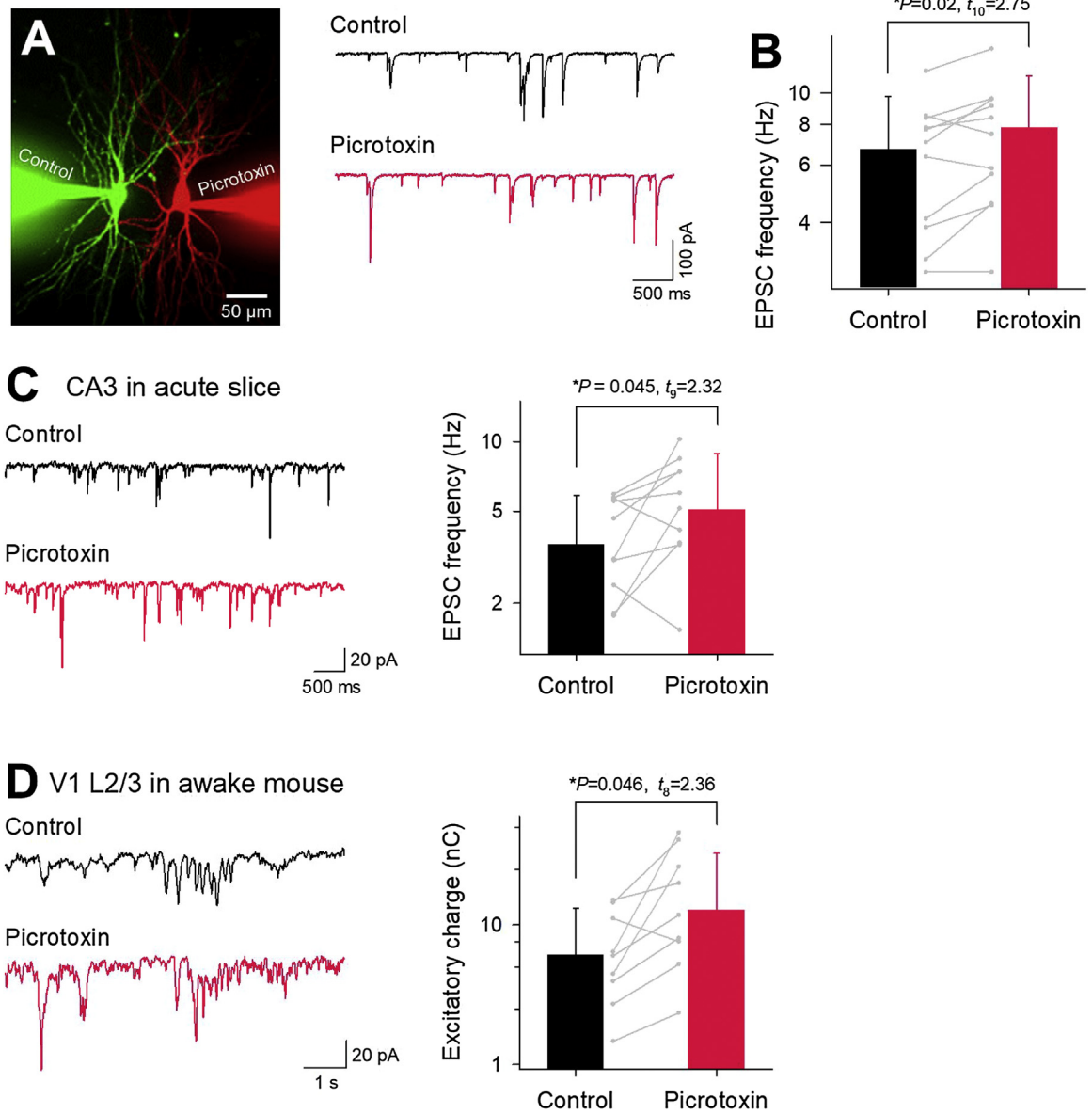


Fig. 6. Blockade of GABA_A receptors increases somatic EPSC frequency. (A) Stacked confocal image of whole-cell recordings from two CA3 pyramidal neurons (left) and traces of spontaneous EPSCs in these neurons (right). One pipette contained 200 μM picrotoxin. Neurons were clamped at –70 mV. (B) Picrotoxin-perfused neurons exhibited higher EPSC frequencies than simultaneously recorded control neurons. The data represent means ± SDs of 11 pairs. Paired *t*-test. (C) Representative traces of paired whole-cell recordings of CA3 neurons in an acute hippocampal slice (left). In each pair, one neuron was intracellularly perfused with 200 μM picrotoxin. Neurons were clamped at –70 mV. Picrotoxin-perfused neurons exhibited higher EPSC frequencies than simultaneously recorded control neurons (right). The data represent means ± SDs of 10 pairs from 10 slices of 9 mice. Paired *t*-test. (D) Representative traces of paired recordings of L2/3 neurons in the primary visual cortex of head-restricted, awake mice (left). In each pair, one neuron was intracellularly perfused with 200 μM picrotoxin. Neurons were clamped at –70 mV. The charge of spontaneous EPSCs is shown on the right. The data represent means ± SDs of 9 pairs from 9 mice. Paired *t*-test.

than the control neurons (Fig. 5E, $P = 2.4 \times 10^{-32}$, $D_{1,882} = 0.30$, Kolmogorov–Smirnov test; control: $n = 1282$ spines in 15 neurons, picrotoxin: $n = 602$ spines in 9 neurons). As described below (Fig. 6), picrotoxin-treated neurons exhibited higher EPSC frequencies, which might affect the chance coincidence between EPSC events and spine activity. Therefore, we also compared the EPSC probabilities corrected by the chance levels of the activity of individual spines. The corrected EPSC probabilities were higher in the picrotoxin-loaded neurons than in the control neurons ($P = 1.9 \times 10^{-4}$, $D_{1,882} = 0.10$). Thus, GABAergic inhibition is likely a factor that reduces the somatic influence of synaptic inputs. On average, the picrotoxin-loaded neurons exhibited slightly smaller EPSC amplitudes (Fig. 5F, $P = 3.2 \times 10^{-12}$, $D_{49,458} = 0.034$, Kolmogorov–Smirnov test; $n = 30,985$ events in 15 neurons, picrotoxin: $n = 18,475$ events

in 9 neurons) and higher EPSC event frequencies than the control neurons (Fig. 5G, $P = 0.017$, $t_{22} = 2.0$, Student's *t*-test). These results suggest that when GABAergic inputs were reduced, even small synaptic inputs became more detectable in the soma.

Similar results were obtained from simultaneously recorded pairs of closely located neurons embedded in the same active network, with one neuron in each pair intracellularly loaded with picrotoxin (Fig. 6A); that is, the picrotoxin-treated neurons exhibited higher EPSC frequencies than the control neurons (Fig. 6B, $P = 0.02$, $t_{10} = 2.75$, paired *t*-test, $n = 11$ pairs). Identical results were obtained for dual recordings from CA3 pyramidal cells in acute hippocampal slices (Fig. 6C, $P = 0.045$, $t_9 = 2.32$, paired *t*-test, $n = 10$ pairs). Moreover, even in layer 2/3 pyramidal cells of the primary visual cortex in awake mice *in vivo*, intracellular picrotoxin

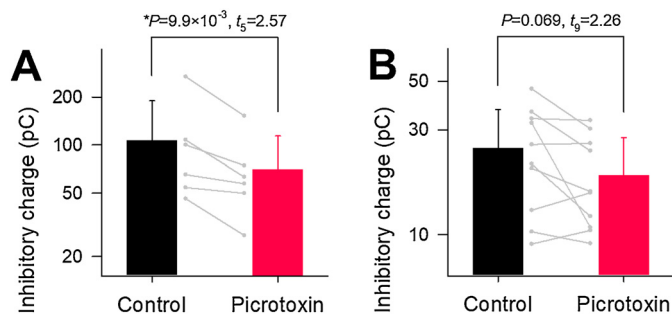


Fig. 7. Blockade of GABA_A receptors reduces somatic inhibitory charges. (A) Picrotoxin-perfused neurons exhibited higher inhibitory charges than simultaneously recorded control neurons in cultured hippocampal slices. Error bars are SDs of 6 pairs. Paired *t*-test. Neurons were clamped at 0 mV. (B) Same as A but for the charges of spontaneous IPSCs in acute hippocampal slices. Error bars are SDs of 7 pairs from 6 mice. Paired *t*-test. Neurons were clamped at 0 mV.

increased the charges of spontaneous EPSCs (Fig. 6D, $P=0.046$, $t_8=2.36$, paired *t*-test, $n=9$ pairs).

A recent study has reported that intracellular perfusion of picrotoxin is not functional (Atherton et al., 2016). However, the concentration of picrotoxin was different from that used in our study and other studies (Inomata et al., 1988; Nelson et al., 1994; Yazaki-Sugiyama et al., 2009). Moreover, we confirmed that our picrotoxin treatment reduced somatic inhibitory charges in picrotoxin-loaded neurons compared to those in simultaneously recorded control neurons in both cultured hippocampal slices (Fig. 7A) and acute hippocampal slices (Fig. 7B).

To quantify the effect of GABAergic inputs, we modeled a conductance-based neuron using the NEURON simulator featured with the morphology of a CA3 pyramidal cell (Fig. 8A). The locus of an excitatory input was fixed at a distance of 405 μm from the soma, and the AMPA and NMDA receptor conductances were set at 1.0 nS and 0.2 nS, respectively. We then scrutinized how the excitation reached the soma when the loci, timings and strengths of inhibitory inputs differed. Specifically, we placed an inhibitory input on various locations over dendrites while placing an excitatory input in the fixed location (Fig. 8A, B, and E) or applied it at various timings relative to an excitatory input (Fig. 8C, D, F, and G) to examine how the inhibitory input modulates the somatic influence of the excitatory input. When there was no time difference between the excitatory and inhibitory inputs, the somatic EPSCs were severely attenuated if inhibitory inputs occurred within approximately 100–200 μm of the excitatory input (Fig. 8A and B). When inhibition occurred at the same site as excitation, the somatic EPSCs were severely reduced at time differences of less than approximately 20–50 ms (Fig. 8C). Stronger inhibition induced larger reductions in EPSCs, and weaker inhibition needed to be more tightly time-locked to the excitation to attenuate the EPSCs (Fig. 8D). Although this simulation was conducted in the voltage-clamp configuration, similar results were obtained for the current-clamped NEURON (Fig. 8E–G). Thus, timely local inhibition efficiently masks the influence of excitatory inputs.

3.3. Dendrites filter presynaptic neuron ensembles

Finally, we examined the relationship between synchronized inputs and the occurrence of detectable EPSCs because neuronal network activity is often coordinated with synchronized spikes of subgroups of neurons referred to as cell assemblies (Takahashi et al., 2010). As expected, the EPSC probabilities increased with the number of simultaneously occurring calcium events; greater synchronization was more likely to elicit EPSCs in the soma (Fig. 9A left), and *vice versa*; thus, larger EPSC charges were associated with more coactive spines (Fig. 9A middle). The EPSC charges were also correlated with the summation of the areas under the curves of the

calcium transients (Fig. 9A right). It is noteworthy that Fig. 9A left shows that the EPSC probabilities were saturated at approximately 80% and did not reach 100% even for large synchronization that recruited more than four spines. These results suggest that there were some synchronized assemblies that did not induce somatic EPSCs. This conclusion is supported by the matrix of joint EPSC probabilities between spines that emitted synchronized activity (Fig. 9B), which indicates that the EPSC probability of a spine varies depending on the combination of other spines that were synchronized with it.

To identify the synchronous ensembles of spines that were coupled or uncoupled to EPSCs, we employed the affinity-propagation clustering algorithm and defined the sets of spines that frequently emitted synchronized calcium events (Frey and Dueck, 2007; Takahashi et al., 2010). We then tried to determine the model that explains the contributions of the activity of individual spine sets to somatic EPSCs. We used two Bayesian logistic regression models, *i.e.*, linear ($\alpha + \beta$) and nonlinear ($\alpha + \beta + \gamma$) models, in which the values of the coefficients β_n and γ_n are positive when the spine set n contributes to somatic EPSCs (Fig. 9C). The Bayesian information criteria were lower in the $\alpha + \beta$ model than in the $\alpha + \beta + \gamma$ model (Fig. 9C; $P=4.2 \times 10^{-8}$, $t_{13}=11.3$, paired *t*-test). Thus, the $\alpha + \beta$ model provides a better explanation of the observed results. In other words, introducing the nonlinear term (γ_n) did not improve the description of EPSC behaviors, which suggests that dendrites basically sum synaptic inputs in a linear manner (Cash and Yuste, 1999). We thus employed the $\alpha + \beta$ model in the following analysis.

The β values of the spine sets conformed to a bimodal Gaussian function with two peaks at 0.02 ± 0.05 and 0.22 ± 0.14 (Fig. 9D; mean \pm SD, $P=2.2 \times 10^{-45}$, least-square fit), which indicates that the spine sets were separable into two distinct groups: sets that significantly contribute to somatic EPSCs and sets that do not significantly contribute. Based on the statistical significance against the null hypothesis $\beta = 0$, we divided the individual sets into significant assemblies ($\beta > 0$) and nonsignificant assemblies ($\beta \approx 0$). Fig. 9E displays the spatial distribution of four representative spine sets in a single neuron, including two sets with $\beta > 0$ and two sets with $\beta \approx 0$. On average, $62 \pm 11\%$ of the spine sets in a single neuron were $\beta > 0$, whereas the remaining $38 \pm 11\%$ were $\beta \approx 0$ (mean \pm SEM of 14 neurons). The mean path distances of the spines from the soma did not differ between the sets with $\beta > 0$ and $\beta \approx 0$ (Fig. 9F; $P=0.26$, $U=607$, Mann-Whitney *U*-test, $\beta > 0$: $n=29$ sets, $\beta \approx 0$: $n=15$ sets). We previously demonstrated that calcium events in spines are often synchronized within 10 μm ; these synchronized events are termed assemblies (Takahashi et al., 2010). The numbers of assemblies emitted from sets with $\beta > 0$ did not differ from those with $\beta \approx 0$ (Fig. 9G; $P=0.24$, $U=700$). These results again confirm that the location of spine activity does not determine the EPSC probability. Finally, the amplitudes of calcium transients in spines with $\beta > 0$ were larger than those with $\beta \approx 0$ (Fig. 9H; $P=3.5 \times 10^{-6}$, $t_{66}=5.06$).

4. Discussion

We developed our calcium imaging technique, which enabled us to record calcium activity in hundreds of spines at a millisecond-resolution. Using this technique, we imaged excitatory synaptic inputs on spines while simultaneously recording somatic postsynaptic currents with whole-cell patch-clamp recording. We observed that excitatory synaptic inputs to dendrites did not consistently affect the cell body. A fraction of the synaptic inputs were not detectable in the cell body. These synaptic inputs became more influential by the blockade of GABAergic inhibition. Our results indicate that a neuron receives synaptic inputs at higher frequencies than the EPSC frequencies estimated in the soma. Moreover,

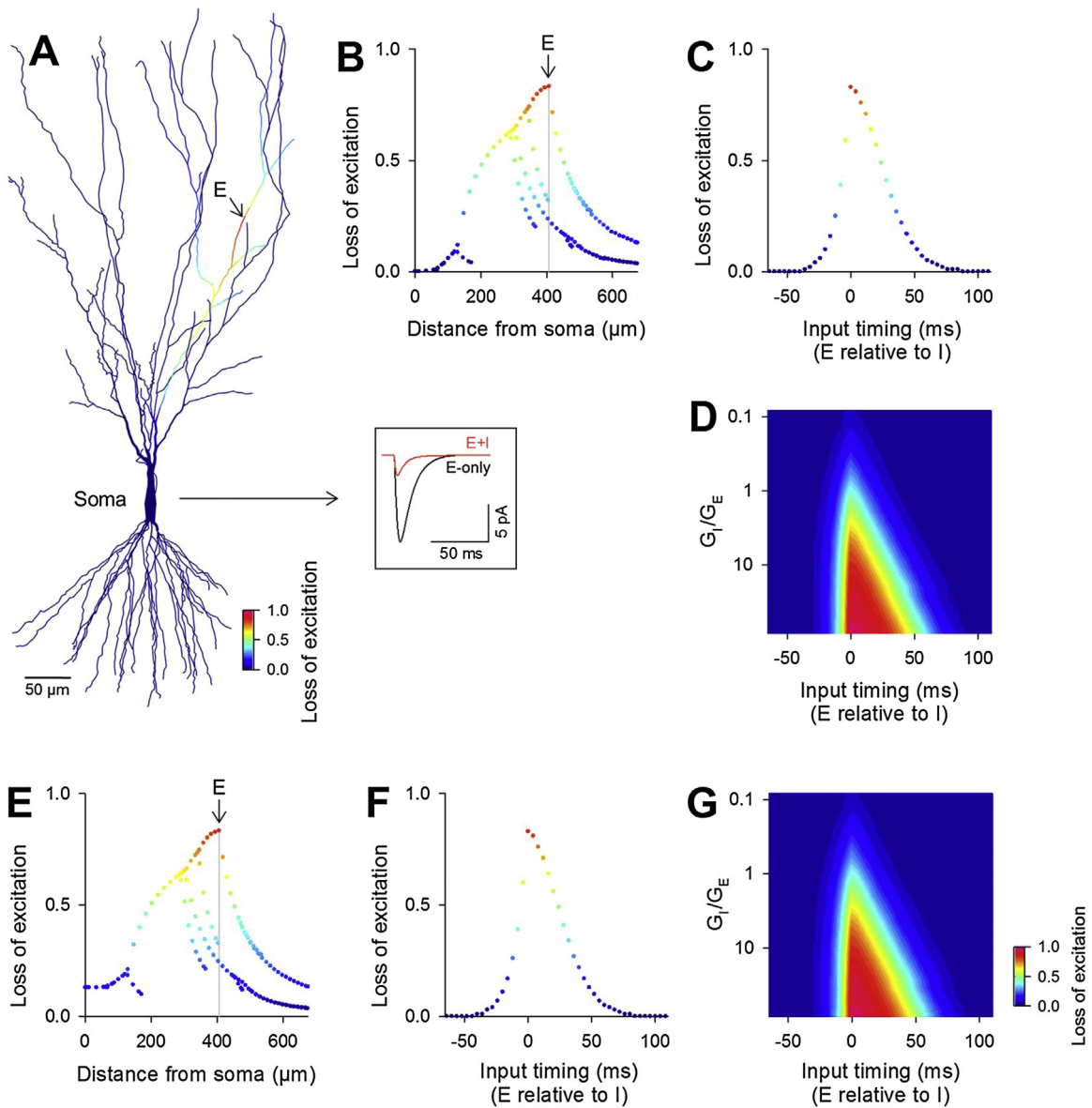


Fig. 8. Precisely timed, local inhibitory inputs can mask excitatory inputs: numerical simulation. (A) Computational NEURON modeling of the spatiotemporal interaction of excitatory and inhibitory inputs. An excitatory input (E) was applied to a dendrite at a path distance of 405 μm from the soma, and an inhibitory input was applied at various sites in the entire cell. The excitatory and inhibitory inputs were simultaneously applied. The pseudocolored diagram indicates the degree of the loss of somatic excitation depending on the location of inhibition relative to somatic excitation without inhibition. The inset traces indicate somatic EPSCs without (*E-only*) and with inhibition applied at the same site as excitation (*E+I*). (B) The same data as A were plotted as a function of the path distance from the soma to inhibitory input sites. (C) Loss of excitation as a function of the time difference between excitation and inhibition, which were both applied at 405 μm from the soma. (D) Two-dimensional plots in the space of the input timing versus the conductance ratio of inhibition to excitation. The pseudocolored scale is identical among the panels A–D. (E–G) The same as B to C but for the neuron model in the current-clamp configuration.

a fraction of synaptic ensembles were likely to be actively filtered out. This finding implies that dendrites screen information from presynaptic neuron assemblies (Fig. 10).

In this study, we imaged synaptic activity from neurons clamped at -30 mV and simultaneously recorded somatic EPSCs by modifying E_{Cl^-} . These conditions may not be physiologically natural, but the EPSC frequencies at -30 mV did not differ from those at -70 mV , and the calcium activity at -30 mV was abolished by NMDA receptor blockade. In addition, dual patch-clamp recordings simultaneously from two neurons and NEURON simulation were both conducted under the resting membrane potentials, replicating our findings of calcium imaging. Thus, we believe that the observed activity reflected physiologically relevant events.

Dendritic computation and its somatic impact have been evaluated mainly using electric, uncaging or optogenetic activation of dendrites, and few studies have addressed the effect under spontaneously active conditions. Neither the scale nor the resolution of the data obtained using conventional techniques is sufficient to strictly associate the timing of individual spine activity with the timing of EPSCs under synaptically noisy conditions. In this study, we improved the optical system of calcium imaging and succeeded in consistently monitoring the activity of more than 200 spines with a millisecond-resolution. This optical technique, combined with the whole-cell recording of somatic EPSCs, enabled the examination of dendritic computation under spontaneous network activity. We observed spine activity exclusively from slice cultures because we

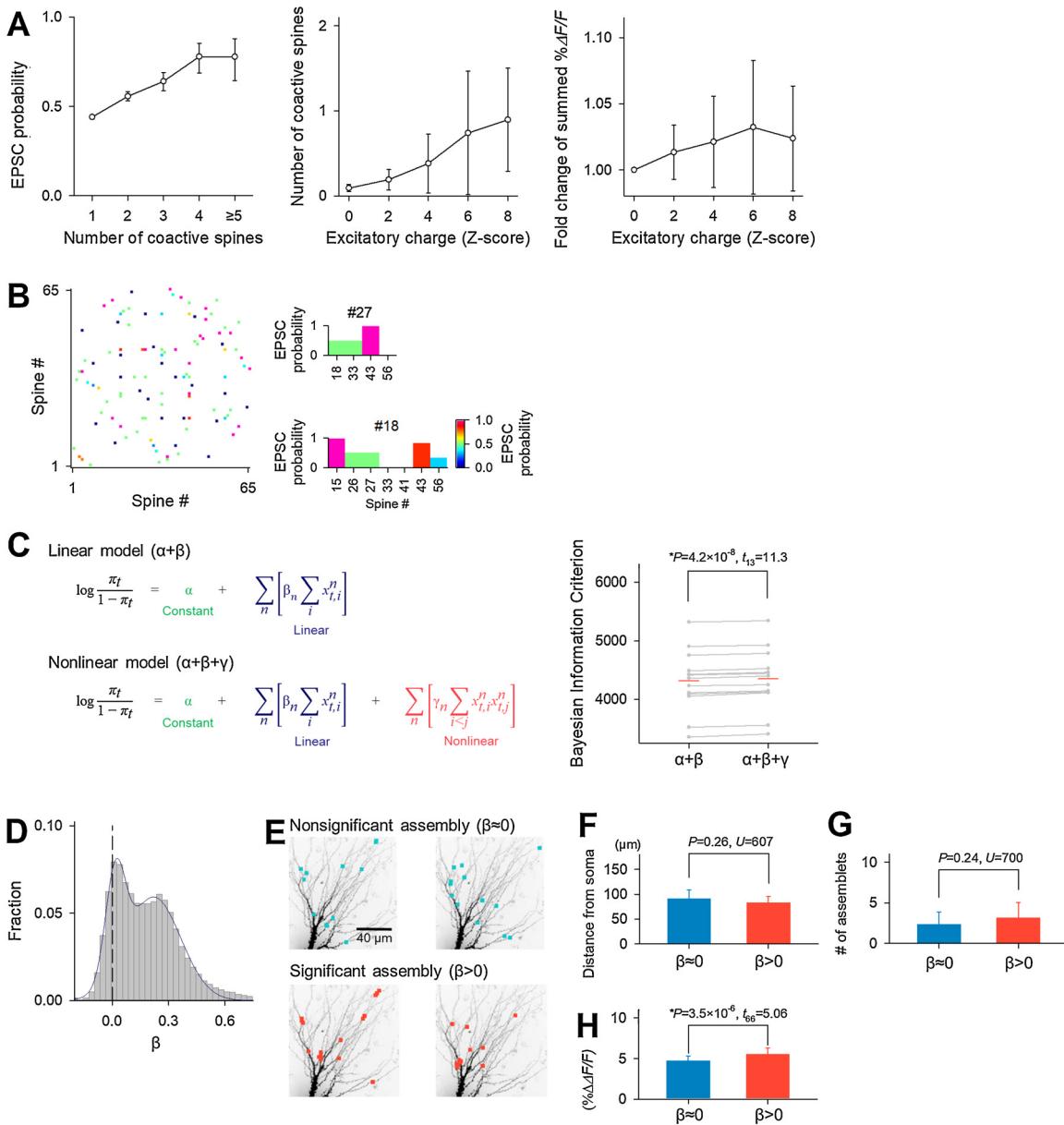


Fig. 9. Dendrites filter presynaptic neuron ensembles. (A) *Left*: Relationship between the synchronization levels in spine activity (the numbers of spines that were coactivated in a bin of 30 ms) and the EPSC probabilities. A total of 10,253 synchronous events were pooled from 15 neurons. The error bars are 95% confidence intervals determined using maximum likelihood estimation. *Middle*: Relationship between somatic excitatory charge and the synchronization level in spine activity. *Right*: Relationship between somatic excitatory charge and the summation of calcium transient in spines. (B) Pseudocolored matrix of conditional EPSC probabilities for all pairs of synchronized spines in a representative neuron. Data for nonsynchronized pairs are shown in white. The right insets illustrate the conditional EPSC probabilities of example spines #18 and #27. (C) The two models ($\alpha + \beta$ and $\alpha + \beta + \gamma$) used for the Bayesian logistic regression of the EPSC probabilities (*left*). The explanatory variable $x_{t,i}^n$ represents the binary state of spine i in spine set n , defined using affinity propagation at time t (active = 1 or non-active = 0). The coefficients β_n and γ_n , respectively, represent the linear and nonlinear effects of spine activity on the EPSC probabilities ($\pi_{t,i}$), and α is constant. Bayesian information criteria (“unfitness” to data) were compared between the $\alpha + \beta$ and $\alpha + \beta + \gamma$ models (*right*, paired t -test, mean \pm SD of 14 neurons). (D) Distribution of β_n in the $\alpha + \beta$ model for individual spine sets defined by affinity propagation repeated with different seeds 1000 times for 14 neurons each. (E) Representative spine sets with β that were significantly higher than zero ($\beta > 0$) or not ($\beta \approx 0$). Only the core spines that were commonly classified as belonging to the same cluster across 1000 iterations of affinity propagation are shown. (F) Path distances to the soma from spines within sets with $\beta \approx 0$ and $\beta > 0$ (Mann-Whitney U -test, mean \pm SD of 9 neurons). (G) Numbers of assemblets (synchronous calcium events that occurred within 10 μ m) emitted by sets with $\beta \approx 0$ and $\beta > 0$. Mann-Whitney U -test. (H) The mean amplitudes of calcium transients in sets with $\beta > 0$ were larger than those with $\beta \approx 0$. Student’s t -test.

failed to conduct the same experiments using acute slice preparations; the less transparent tissues of the acute slices hindered the large-scale, high-speed optical imaging of spine calcium dynamics. Moreover, the spontaneous activity of spines located close to the slice surface in acute slices was extremely sparse because the slicing procedure severed a large number of near-surface axons. In slice cultures, the microcircuits may be aberrantly reorganized to some extent, but, the basic circuit structures are preserved, and the level and patterns of the overall activity in cultured networks resemble

those of *in vivo* spontaneous activity (Okamoto et al., 2014; Takahashi et al., 2012, 2010).

Cable theory predicts that the electric influence of synaptic activity is reduced along a longitudinal axis of dendrites (Rall, 1959). Thus, the distal activity of spines located further from the soma may have a higher likelihood of undetectable EPSCs. However, the EPSC probability did not depend on the location of the spines. Our data indicate that neither the morphology nor the location of a spine is a major determinant of the somatic EPSC amplitude and

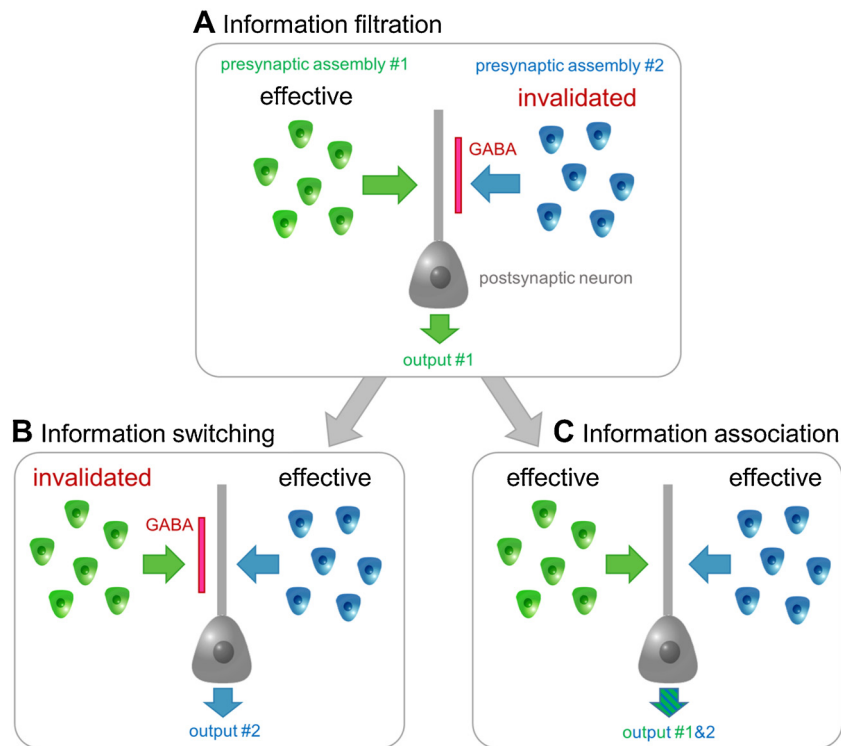


Fig. 10. Schematic illustrations of the putative function of dendritic filtering of presynaptic neuron ensembles. (A) Synaptic inputs from neuron assembly #1 can activate the postsynaptic neuron, whereas synaptic inputs from assembly #2 are invalidated by dendritic GABAergic inputs and cannot influence the output of the postsynaptic neuron. (B) The same as (A), but GABAergic inputs invalidate assembly #1. Thus, the postsynaptic neuron conveys information about assembly #2. (C) Information on both assemblies is mixed when the GABAergic influence vanishes. The authors speculate that dendritic filtering enables a rapid switch of information flow routes (B) and an admixture of different information (C) even without large-scale rewiring of excitatory connections.

that the effects of such structural variations are practically negligible under a large variety of spontaneous synaptic bombardments.

Dendrites receive spatiotemporally clustered inputs and perform a nonlinear integration of synaptic inputs (Losonczy and Magee, 2006; Takahashi et al., 2012). Therefore, individual dendritic segments can act as computational units (Branco and Hausser, 2010). We thus reasoned that spines that exhibited similar EPSC probabilities were localized in the same vicinity. However, the path distances between spines were not correlated with the differences in their EPSC probabilities. Rather, spines with various EPSC probabilities seemed to be distributed over dendrites without apparent spatial rules. However, effective inputs were slightly more clustered than the ineffective inputs, although coactive spines during both effective and ineffective inputs were spatially clustered to a similar extent. These results indicate that locally synchronized synaptic inputs may partly explain the stochastic detectability of the EPSCs.

The blockade of GABA_A receptor activity increased the EPSC probability and enhanced the amplitudes of calcium transients, but it did not affect the spine activity frequency. The intracellular perfusion of picrotoxin also increased the EPSC frequency. Therefore, GABAergic inhibition is at least one of the factors that contribute to the reduction of the somatic impact of individual synaptic inputs, although these results do not exclude the involvement of other factors. Even in the picrotoxin-loaded neurons, a portion of the synaptic inputs were not recorded with somatic EPSCs. This partial effect may also imply the involvement of miniature synaptic inputs or other types of ion channels other than GABA_A receptors, such as voltage-gated potassium channels (Hu et al., 2007).

Our numerical simulation predicts that precisely timed local GABAergic inputs are necessary to cancel out the somatic effects of excitatory inputs and that GABAergic inputs to the soma or different branches are insufficient to invalidate EPSCs. Consistent with this

prediction, EPSC-coupled inputs induced larger calcium transients than EPSC-uncoupled inputs in the same spines. This result suggests that inhibition occurs near the activated spines. We speculate that excitatory inputs are mainly silenced by timely local inhibition. Previous studies have demonstrated the existence of such local inhibition (Liu, 2004) and have shown that local inhibition reduces calcium influx into spines (Chiu et al., 2013; Mullner et al., 2015) and modulates synaptic plasticity (Hayama et al., 2013). However, these studies focused mainly on the role of local inhibition on calcium dynamics in spines, and the mechanisms by which local inhibition affects neural network computation remain unclear. The effect of local inhibition on dendritic integration has been examined using *in silico* modeling (Gidon and Segev, 2012; Hao et al., 2009) or artificially evoked synaptic inputs (Liu, 2004; Muller et al., 2012), but to our knowledge, no study has addressed the role of local inhibition on dendritic integration in a spontaneous active network.

Network activity is coordinated with synchronous spikes emitted by cell assemblies, which are putative functional units of neuronal information (Harris, 2005; Morris, 1999; Takahashi et al., 2010). This study demonstrates that synaptic activities over dendritic trees are often synchronized within specific sets of spines and may be separated using an unsupervised clustering method, which indicates that a single neuron receives synaptic inputs from different cell assemblies. This mixed wiring feature may provide a structural platform to induce a dramatic switching of the information flow pathway (Fig. 10B) and integrate different information contents during associative learning (Fig. 10C).

In conclusion, we found that a fraction of synaptic inputs were not detectable in the cell body. Reduced GABAergic inhibition partially restored the influences of synaptic inputs on somatic excitation. In general, dendrites code synaptic inputs from millions of presynaptic neurons. Dendrites may preferentially pass necessary

information to the soma *via* mechanisms consisting of GABAergic inhibition. Our imaging technique will enable us to approach this enigmatic process.

Author contributions

C.K. and Y.I. designed the study. C.K., H.U., Y.M. and Y.I. wrote the manuscript. C.K. and T.I. conducted the calcium imaging. C.K., K.O., and K.F. conducted the electrophysiological experiments. C.K., T.K. and O.A. conducted the super resolution imaging. H.U. conducted computational modeling. Y.M. and C.K. conducted regression analysis. A.F.S. engineered the software calcium imaging analysis. All authors discussed the results and commented on the manuscript. All authors have read and approved the submission of this article.

Competing financial interests

The authors declare that there are no competing financial interests.

Acknowledgements

We are grateful to Dr. Shigeru Shinomoto for his technical comments on the data analysis. This work was supported by Grants-in-Aid for Scientific Research (18H05114) and the Human Frontier Science Program (RGP0019/2016). This work was conducted partly as a program at the International Research Center for Neurointelligence (WPI-IRCN) of the University of Tokyo Institutes for Advanced Study at the University of Tokyo.

References

Atherton, L.A., Burnell, E.S., Mellor, J.R., 2016. Assessment of methods for the intracellular blockade of GABA_A receptors. *PLoS One* 11, e0160900.

Baker, J.L., Perez-Rosello, T., Migliore, M., Barriounevo, G., Ascoli, G.A., 2011. A computer model of unitary responses from associational/commissural and perforant path synapses in hippocampal CA3 pyramidal cells. *J. Comput. Neurosci.* 31, 137–158.

Branco, T., Hausser, M., 2010. The single dendritic branch as a fundamental functional unit in the nervous system. *Curr. Opin. Neurobiol.* 20, 494–502.

Cash, S., Yuste, R., 1999. Linear summation of excitatory inputs by CA1 pyramidal neurons. *Neuron* 22, 383–394.

Chiu, C.Q., Lur, G., Morse, T.M., Carnevale, N.T., Ellis-Davies, G.C., Higley, M.J., 2013. Compartmentalization of GABAergic inhibition by dendritic spines. *Science* 340, 759–762.

Eccles, J.C., 1964. *The Physiology of Synapses*. Springer-Verlag, Berlin.

Forti, L., Bossi, M., Bergamaschi, A., Villa, A., Malgaroli, A., 1997. Loose-patch recordings of single quanta at individual hippocampal synapses. *Nature* 388, 874–878.

Frey, B.J., Dueck, D., 2007. Clustering by passing messages between data points. *Science* 315, 972–976.

Funayama, K., Minamisawa, G., Matsumoto, N., Ban, H., Chan, A.W., Matsuki, N., Murphy, T.H., Ikegaya, Y., 2015. Neocortical rebound depolarization enhances visual perception. *PLoS Biol.* 13, e1002231.

Gidon, A., Segev, I., 2012. Principles governing the operation of synaptic inhibition in dendrites. *Neuron* 75, 330–341.

Hao, J., Wang, X.D., Dan, Y., Poo, M.M., Zhang, X.H., 2009. An arithmetic rule for spatial summation of excitatory and inhibitory inputs in pyramidal neurons. *Proc. Natl. Acad. Sci. U. S. A.* 106, 21906–21911.

Harris, K.D., 2005. Neural signatures of cell assembly organization. *Nat. Rev. Neurosci.* 6, 399–407.

Hastie, T., Tibshirani, R., Friedman, J.H., 2009. *The Elements of Statistical Learning: Data Mining, Inference, and Prediction*, 2nd ed. Springer, New York.

Hayama, T., Noguchi, J., Watanabe, S., Takahashi, N., Hayashi-Takagi, A., Ellis-Davies, G.C., Matsuzaki, M., Kasai, H., 2013. GABA promotes the competitive selection of dendritic spines by controlling local Ca²⁺ signaling. *Nat. Neurosci.* 16, 1409–1416.

Hines, M.L., Carnevale, N.T., 1997. The NEURON simulation environment. *Neural Comput.* 9, 1179–1209.

Hu, H., Vervaeke, K., Storm, J.F., 2007. M-channels (Kv7/KCNQ channels) that regulate synaptic integration, excitability, and spike pattern of CA1 pyramidal cells are located in the perisomatic region. *J. Neurosci.* 27, 1853–1867.

Iacaruso, M.F., Gasler, I.T., Hofer, S.B., 2017. Synaptic organization of visual space in primary visual cortex. *Nature* 547, 449–452.

Inomata, N., Tokutomi, N., Oyama, Y., Akaike, N., 1988. Intracellular picrotoxin blocks pentobarbital-gated Cl⁻ conductance. *Neurosci. Res.* 6, 72–75.

Koyama, R., Muramatsu, R., Sasaki, T., Kimura, R., Ueyama, C., Tamura, M., Tamura, N., Ichikawa, J., Takahashi, N., Usami, A., Yamada, M.K., Matsuki, N., Ikegaya, Y., 2007. A low-cost method for brain slice cultures. *J. Pharmacol. Sci.* 104, 191–194.

Liu, G., 2004. Local structural balance and functional interaction of excitatory and inhibitory synapses in hippocampal dendrites. *Nat. Neurosci.* 7, 373–379.

London, M., Hausser, M., 2005. Dendritic computation. *Annu. Rev. Neurosci.* 28, 503–532.

Losonczy, A., Magee, J.C., 2006. Integrative properties of radial oblique dendrites in hippocampal CA1 pyramidal neurons. *Neuron* 50, 291–307.

Mainen, Z.F., Sejnowski, T.J., 1996. Influence of dendritic structure on firing pattern in model neocortical neurons. *Nature* 382, 363–366.

Major, G., Larkum, M.E., Schiller, J., 2013. Active properties of neocortical pyramidal neuron dendrites. *Annu. Rev. Neurosci.* 36, 1–24.

Migliore, M., Shepherd, G.M., 2002. Emerging rules for the distributions of active dendritic conductances. *Nat. Rev. Neurosci.* 3, 362–370.

Morris, R.G., 1999. D.O. Hebb: The Organization of Behavior, Wiley: New York; 1949. *Brain Res Bull* 50, 437.

Muller, C., Beck, H., Coulter, D., Remy, S., 2012. Inhibitory control of linear and supralinear dendritic excitation in CA1 pyramidal neurons. *Neuron* 75, 851–864.

Mullner, F.E., Wierenga, C.J., Bonhoeffer, T., 2015. Precision of inhibition: dendritic inhibition by individual GABAergic synapses on hippocampal pyramidal cells is confined in space and time. *Neuron* 87, 576–589.

Nelson, S., Toth, L., Sheth, B., Sur, M., 1994. Orientation selectivity of cortical neurons during intracellular blockade of inhibition. *Science* 265, 774–777.

Okamoto, K., Ishikawa, T., Abe, R., Ishikawa, D., Kobayashi, C., Mizunuma, M., Norimoto, H., Matsuki, N., Ikegaya, Y., 2014. Ex vivo cultured neuronal networks emit in vivo-like spontaneous activity. *J. Physiol. Sci.* 64, 421–431.

Rall, W., 1959. Branching dendritic trees and motoneuron membrane resistivity. *Exp. Neurol.* 1, 491–527.

Reyes, A., 2001. Influence of dendritic conductances on the input-output properties of neurons. *Annu. Rev. Neurosci.* 24, 653–675.

Safiullina, V.F., Caiati, M.D., Sivakumaran, S., Bisson, G., Migliore, M., Cherubini, E., 2010. Control of GABA release at mossy fiber-CA3 connections in the developing Hippocampus. *Front. Synaptic Neurosci.* 2, 1.

Sasaki, T., Matsuki, N., Ikegaya, Y., 2011. Action-potential modulation during axonal conduction. *Science* 331, 599–601.

Spruston, N., 2008. Pyramidal neurons: dendritic structure and synaptic integration. *Nat. Rev. Neurosci.* 9, 206–221.

Stuart, G.J., Spruston, N., 2015. Dendritic integration: 60 years of progress. *Nat. Neurosci.* 18, 1713–1721.

Szymanska, A.F., Kobayashi, C., Norimoto, H., Ishikawa, T., Ikegaya, Y., Nenadic, Z., 2016. Accurate detection of low signal-to-noise ratio neuronal calcium transient waves using a matched filter. *J. Neurosci. Methods* 259, 1–12.

Takahashi, N., Sasaki, T., Matsumoto, W., Matsuki, N., Ikegaya, Y., 2010. Circuit topology for synchronizing neurons in spontaneously active networks. *Proc. Natl. Acad. Sci. U. S. A.* 107, 10244–10249.

Takahashi, N., Kitamura, K., Matsuo, N., Mayford, M., Kano, M., Matsuki, N., Ikegaya, Y., 2012. Locally synchronized synaptic inputs. *Science* 335, 353–356.

Yazaki-Sugiyama, Y., Kang, S., Cateau, H., Fukai, T., Hensch, T.K., 2009. Bidirectional plasticity in fast-spiking GABA circuits by visual experience. *Nature* 462, 218–221.